

# Flow birefringence of shear-thinning fluid in a Hele-Shaw cell

Misa Kawaguchi<sup>1</sup>, William Kai Alexander Worby<sup>1</sup>, Yuto Yokoyama<sup>2</sup>,  
Ryuta X. Suzuki<sup>3</sup>, Yuichiro Nagatsu<sup>4</sup>, Yoshiyuki Tagawa<sup>1,5\*</sup>

Received: date / Accepted: date

**Abstract** Flow birefringence measurement is an emerging technique for visualizing stress fields in fluid flows. This study investigates flow birefringence in the steady radial Hele-Shaw flow of a shear-thinning fluid. In this flow configuration, stress is dominant along the optical axis, challenging the applicability of the conventional stress-optic law (SOL). We conduct flow birefringence measurements at various flow rates and compare the results with theoretical predictions. The observed phase retardation cannot be quantitatively explained using the conventional SOL, but is successfully described using the second-order SOL, which accounts for stress along the optical direction, using the results of rheo-optical measurements. Furthermore, we investigate the shear-thinning effects on phase retardation from two perspectives: (i) stress changes resulting from viscosity variations and (ii) the variation of the shear-dependent stress-optic coefficient in the second-order SOL. Our findings indicate that the latter is more significant and shear-thinning behavior suppresses radial variations in phase retardation. This study demonstrates that the combination of the second-order SOL and rheo-optical measurements is essential for an accurate interpreta-

tion of flow birefringence in Hele-Shaw flow, providing a noninvasive approach for stress field analysis in high-aspect-ratio geometries.

## 1 Introduction

Suspensions of crystal-like particles or polymers generate flow birefringence (double refraction) when a velocity gradient is applied (Maxwell, 1874). Flow birefringence is a useful tool for visualizing flow patterns and understanding the rheology of complex fluids. In the absence of flow, the suspension is optically isotropic because nonspherical particles or polymers are randomly oriented due to Brownian motion. When flow is applied, local velocity gradients induce particle alignment, and this leads to an optically anisotropic state in the fluid. These properties are exploited for flow visualization in biomechanics (Rankin et al., 1989; Sun et al., 1999; Sun and Huang, 2016) and biolocomotion (Hu et al., 2009). Using the optical anisotropy induced by the alignment of suspended particles, flow birefringence has been applied to rheo-optic measurements (Ober et al., 2011; Sato et al., 2024; Worby et al., 2024), which enable the study of macromolecules (Cerf and Scheraga, 1952).

Flow birefringence can also be used in the experimental determination of shear rate and stresses based on the stress-optic law (SOL) (Aben and Guillemet, 1993), which expresses the relationship between birefringence and stresses. Studies of flow birefringence using the SOL have mostly considered two-dimensional flow (Noto et al., 2020) or uniform shear flow (Decruppe and Ponton, 2003; Lane et al., 2022; Worby et al., 2024). The conventional approach for obtaining the stress field is to obtain velocity measurements, such as through particle image velocimetry (Kloosterman et al., 2011;

1: Department of Mechanical Systems Engineering, Tokyo University of Agriculture and Technology, Koganei, Tokyo 184-8588, Japan

2: Micro/Bio/Nanofluidics Unit, Okinawa Institute of Science and Technology, Kunigami-gun, Okinawa 904-0495, Japan

3: West Tokyo Joint Center for Sustainability Research and Implementation, Tokyo University of Agriculture and Technology, Koganei, Tokyo 184-8588, Japan

4: Department of Chemical Engineering, Tokyo University of Agriculture and Technology, Koganei, Tokyo 184-8588, Japan

5: Institute of Global Innovation Research, Tokyo University of Agriculture and Technology, Koganei, Tokyo 184-8588, Japan

\* E-mail: tagawayo@cc.tuat.ac.jp

Ehyaie and Kiger, 2014). However, predicting the shear stresses in thin flow regions or for non-Newtonian fluids remains challenging.

One example of confined thin flow is Hele-Shaw flow, which occurs in the thin space between two parallel plates. Hele-Shaw flow can be used to visualize the streamlines of two-dimensional Euler flows (Hele-Shaw, 1898; Batchelor, 2000), to study the Saffman–Taylor instability (Homsy, 1987; Saffman and Taylor, 1958), to examine biological phenomena such as cell adhesion (Rezania et al., 1997; Goldstein and DiMilla, 1998; DeIon et al., 2020), and to evaluate cleaning processes (Deshmukh et al., 2022). Thus, the measurement of the stress field in a Hele-Shaw cell is important in understanding mechanobiology, the fluid mechanics of instability phenomena, and cleaning processes.

There are several unsolved problems regarding flow birefringence measurements in a Hele-Shaw cell, such as the shear rate and stress field evaluation. First, the dominant components of stress in Hele-Shaw flow are not included in the conventional SOL. The conventional SOL is not sufficient to understand the three-dimensional phenomena that occur in such as Hele-Shaw flow and rectangular channels. Nakamine et al. (2024) suggested that the second-order SOL (explained in §2.1) has the potential to explain the effects of stress along the optical axis.

Second, the gap in a Hele-Shaw cell is small and the resulting integrated length and integrated value of the photoelasticity along the gap become small. One possible solution to this problem is to use a high-sensitivity birefringent material. Another solution to overcome weak detection due to the small integrated length is to use a relatively high-concentration suspension with birefringent material. However, increasing the concentration of the birefringent material enhances the shear-thinning of the suspension. To date, the working fluid has been assumed to be Newtonian (Nakamine et al., 2024; Worby et al., 2024), and it is unclear how non-Newtonian effects will influence flow birefringence in terms of the second-order SOL.

The purpose of this study is to investigate flow birefringence in steady radial Hele-Shaw flow, focusing on the effects of stress along the optical axis and the non-Newtonian properties of the fluid. We conduct flow birefringence measurements using cellulose nanocrystal (CNC) suspensions over a range of flow rates, and compare the results with theoretical predictions based on the second-order SOL. Additionally, we discuss two aspects of shear-thinning effects on phase retardation: (i) the change in stress resulting from viscosity variations and (ii) the shear-dependent coefficient in the second-order SOL. We demonstrate that the latter is dominant.

A quantitative explanation of phase retardation in a Hele-Shaw cell is an important step toward our understanding of three-dimensional stress fields. Hele-Shaw cells are often used to study the Saffman–Taylor instability (viscous fingering) (Saffman and Taylor, 1958; Homsy, 1987). Flow birefringence has been used to study other instabilities, such as the elastic instability (Robert et al., 2003) and the stick-slip instability (Zhao et al., 2016). Previous theoretical, experimental, and numerical approaches have found that the three-dimensional structure inside the gap plays an important role in the onset and suppression of viscous fingering (Lajeunesse et al., 1997; Yang and Yortsos, 1997; Lajeunesse et al., 1999; Bischofberger et al., 2014; Oliveira and Meiburg, 2011; Videbæk and Nagel, 2019; Nand et al., 2022). Hele-Shaw cells are not only used to observe the Saffman–Taylor instability, but are also important in studies on multiphase flows (Marin et al., 2015; Zhang and Rallabandi, 2023). These studies illustrate the importance of the three-dimensional flow field in Hele-Shaw flow. In this context, the results presented in this paper contribute to advances in the study of fluid mechanics.

The remainder of this paper is organized as follows. In §2, the principle of the photoelastic technique and the theoretical solution of phase retardation in radial Hele-Shaw flow are introduced. In §3, the experimental setup and preliminary experiments are presented. In §4, the results of phase retardation in Hele-Shaw flow are presented and the applicability of the SOL considering three-dimensional stress fields with non-Newtonian fluid flow is discussed. Finally, the conclusions from this study are summarized in §5.

## 2 Calculation of theoretical phase retardation

In §2.1, we identify the relationship between the stress components and the phase retardation (Nakamine et al., 2024). §2.2 describes the velocity distribution and stress tensor in Hele-Shaw flow. In §2.3, theoretical solutions are obtained under non-Newtonian effects and the coefficient of the second term of the SOL is determined as a function of the shear rate (Worby et al., 2024).

### 2.1 Principle of photoelastic measurement

The quantitative evaluation of flow birefringence requires the second-order SOL to be considered (Nakamine et al., 2024). The second-order SOL relates all components of the stress tensor with the phase retardation, while the first-order SOL neglects the stresses along the optical axis.

Worby et al. (2024) has reported that the coefficient of the second-order stress term is a function of the second invariant of the deformation rate tensor. Here, we derive the second-order SOL for Hele-Shaw flow, where the dominant stress components are different from previous studies, such as for rectangular channel flow and shear flow.

The phase retardation is the integrated value of the birefringence with respect to the optical axis. Thus, the phase retardation  $\Delta$  [nm] is expressed as (Doyle, 1982; Aben and Puro, 1997; Nakamine et al., 2024)

$$\Delta = \sqrt{V_1^2 + V_2^2}, \quad (1)$$

where

$$V_1 = \int (C_1(\sigma_{yy} - \sigma_{xx}) + C_2[(\sigma_{xx} + \sigma_{yy})(\sigma_{yy} - \sigma_{xx}) + \sigma_{yz}^2 - \sigma_{xz}^2]) dz, \quad (2)$$

$$V_2 = \int (2C_1\sigma_{xy} + C_2[2(\sigma_{xx} + \sigma_{yy})\sigma_{xy} + 2\sigma_{xz}\sigma_{yz}]) dz. \quad (3)$$

The optical axis is set to the  $z$ -direction in Cartesian coordinates.  $C_1$  [Pa<sup>-1</sup>] and  $C_2$  [Pa<sup>-2</sup>] are the stress-optic coefficients, and  $\sigma_{ij}$  denotes the stress components. When  $C_2 = 0$ , Eqs. (1)–(3) correspond to the conventional SOL (Prabhakaran, 1975) used in solid mechanics.

The phase retardation  $\Delta$  is obtained from a four-step phase-shifting method (Ramesh, 2021; Otani et al., 1994; Onuma and Otani, 2014). The retardation is calculated as follows using four intensities captured by super-pixels of the image sensor:

$$\Delta = \frac{\lambda}{2\pi} \sin^{-1} \frac{\sqrt{(I'_{90} - I'_0)^2 + (I'_{45} - I'_{135})^2}}{I/2}, \quad (4)$$

where  $\lambda$  is the wavelength of the light and  $I'$  is the intensity detected by the camera sensor through a polarizer; the subscript denotes the angle of the polarizer.  $I$  is the intensity of the incident light, given by

$$I = I'_0 + I'_{45} + I'_{90} + I'_{135}. \quad (5)$$

## 2.2 Radial Hele-Shaw flow

Radial Hele-Shaw flow generates a spatially dependent shear stress. This means it is suitable for validation of the integrated photoelasticity. The configuration and coordinates are shown in Fig. 1. Two parallel plates are

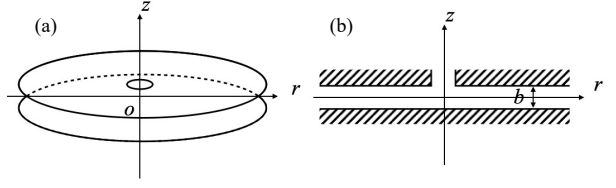


Fig. 1: Configuration and coordinates in radial Hele-Shaw flow

separated by a gap  $b$ . In this study, the only injection point is on the upper side.

The viscosity in a power-law solution is described as (Macosko, 1994; Bird et al., 1987)

$$\eta(\dot{\gamma})_{GNF} = m\dot{\gamma}^{n-1}, \quad (6)$$

where  $m$  and  $n$  are power-law constants, and  $\dot{\gamma}$  is the shear rate. The velocity profile for the non-Newtonian case can be expressed using a power-law solution (Macosko, 1994; Bird et al., 1987) as

$$u_r(r, z) = \frac{Q}{2\pi r b} \frac{2n+1}{n+1} \left(1 - \left|\frac{2z}{b}\right|^{\frac{n+1}{n}}\right), \quad (7)$$

where  $Q$  is the flow rate. Equation (7) is taken from Winter (1975), with the modification of the absolute value in the last term. The absolute value is applied to prevent negative values inside the exponent, ensuring a real-valued result.

The deformation rate tensor  $\mathbf{D}$  and the stress tensor  $\mathbf{T}_{HS}$  in radial Hele-Shaw flow are derived under the assumptions of axial symmetry around the  $z$ -axis,  $u_\theta = 0$ , and  $u_z = 0$ :

$$\mathbf{D} = \frac{1}{2} (\nabla \mathbf{u} + \nabla \mathbf{u}^T) = \begin{pmatrix} \frac{\partial u_r}{\partial r} & 0 & \frac{1}{2} \left(\frac{\partial u_r}{\partial z}\right) \\ 0 & \frac{u_r}{r} & 0 \\ \frac{1}{2} \left(\frac{\partial u_r}{\partial z}\right) & 0 & 0 \end{pmatrix}, \quad (8)$$

$$\mathbf{T}_{HS} = -p\mathbf{I} + 2\mu\mathbf{D} = \begin{pmatrix} -p + 2\mu \frac{\partial u_r}{\partial r} & 0 & \mu \frac{\partial u_r}{\partial z} \\ 0 & -p + 2\mu \frac{u_r}{r} & 0 \\ \mu \frac{\partial u_r}{\partial z} & 0 & -p \end{pmatrix}, \quad (9)$$

where  $\mu$  is the viscosity and  $p$  is the fluid pressure.

### 2.3 Theoretical solution of phase retardation

The theoretical solution of phase retardation is calculated based on Eqs. (1)–(3) using the stress components in Eq. (9). Here,  $C_1$  is set to  $1.0 \times 10^{-5}$ , which is similar to the expectation based on the data presented by Nakamine et al. (2024) in their Fig. 13(a). This is reasonable because the contribution of the term with  $C_1$  is negligible in Hele-Shaw flow. The stress-optic component of  $C_2$  for Eq. (2) is obtained from rheo-optic measurements (see §3.2.1). The shear-thinning effects are considered in the velocity (Eq. (7)) and viscosity in the stress tensor (Eq. (9)). For the former, the shear viscosity is fitted using a power-law model. The power-law coefficients  $m = 8.7429$  and  $n = 0.8951$  are used in Eq. (7). For the latter, the shear viscosity is fitted using the Carreau–Yasuda model (Yasuda et al., 1981).

Different viscosity models are used because there is no theoretical framework considering the Carreau–Yasuda model for the velocity, and using a power-law model for the velocity and the Carreau–Yasuda model for the viscosity in the stress tensor provides a reasonable approach.

## 3 Experiments

§3.1 explains the experimental setup. In §3.1.1, the test fluid preparation and its properties are described. §3.1.2 explains the experimental setup using a Hele-Shaw cell to measure the phase retardation. §3.2 describes the preliminary experiments. §3.2.1 explains the use of rheo-optical measurements to determine  $C_2$  for the theoretical retardation. In §3.2.2, explains the phase retardation measurements using Hele-Shaw cell to evaluate time history of phase retardation. In §3.2.3, an actual gap with flow in the Hele-Shaw cell is discussed in detail based on the results for the interface velocity.

### 3.1 Experimental methods

#### 3.1.1 Solution preparation

The CNC (cellulose nanocrystal high sulfonic group content, freeze-dried (CNC-HSFD), Cellulose Lab) was dispersed in ultrapure water (Milli-Q, Merck) as a birefringent material. There are many birefringent materials, such as tobacco mosaic virus (Hu et al., 2009), milling yellow (Pindera and Krishnamurthy, 1978), CNC (Lane et al., 2024), and KaleidoFlow (Noto et al., 2020). Our group examined several birefringent materials, and

selected CNC-HSFD as a high-sensitivity example from among the materials currently available.

The concentration of the CNC was set to 3 wt%. If the CNC concentration is less than 3 wt% under our conditions, the flow birefringence becomes too weak to detect and is hidden within the noise. The CNC suspension was sonicated using a homogenizer (UX-300, Mitsui Electric) to ensure that the particles were homogeneously dispersed. Ultrasound treatment was applied for 400 s (on time: 5 s, off time: 10 s, set time: 200 s  $\times$  two sets) at 40 % power in an ice bath to prevent overheating.

The shear viscosity was measured by a rheometer (MCR302, Anton Paar) equipped with a cone-plate (CP50-0.5, Anton Paar) at 20°C (Fig. 2), as controlled by a temperature system in the rheometer. Before sonication, the CNC suspension exhibited pronounced shear-thinning due to the CNC particles. After sonication, the shear-thinning of the CNC suspension was suppressed and the shear viscosity had decreased, as observed in a previous study (Shafei-Sabet et al., 2012).

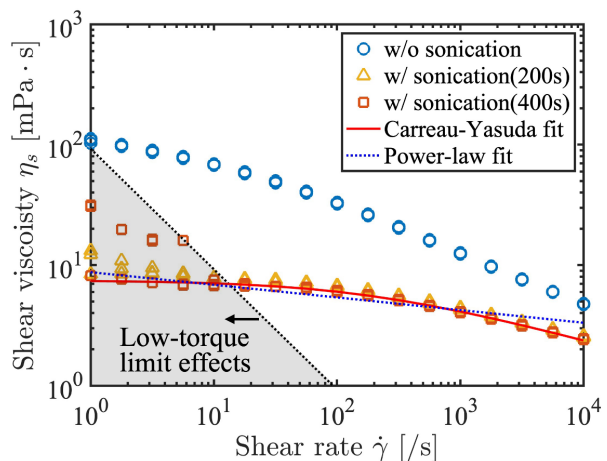


Fig. 2: (a) Shear viscosity measured by rheometer at 20°C; measurements were repeated three times for each condition. Blue circles: No sonication; Yellow triangles: Sonication for 200 s; Red squares: Sonication for 400 s. Black dotted line indicates lower-torque limit. Blue dotted line is the fitting curve using the power-law model of Eq. (6) with  $m = 8.7429$  and  $n = 0.8951$ . Red solid line is the fitting curve using the Carreau–Yasuda model (Eq. (10)) for data with 400 s sonication in the range of  $\dot{\gamma} > 10$

The shear-thinning property of the working fluid was considered in the stress tensor (Eq. (9)) by fitting the shear curve measured by the rheometer. The Carreau–Yasuda model (Yasuda et al., 1981) was in-

roduced for fitting and the following parameters were used to obtain the theoretical flow birefringence from the measured data:

$$\eta_{CY} = \eta_{\infty} + (\eta_0 - \eta_{\infty})[1 + (\lambda\dot{\gamma})^a]^{\frac{N-1}{a}}, \quad (10)$$

$$\begin{aligned} \dot{\gamma} &= \sqrt{2(\mathbf{D} : \mathbf{D})} \\ &= \sqrt{2\left(\frac{\partial u_r}{\partial r}\right)^2 + 2\left(\frac{u_r}{r}\right)^2 + \left(\frac{\partial u_r}{\partial z}\right)^2}, \end{aligned} \quad (11)$$

where  $\eta_{\infty} = -0.1427$ ,  $\eta_0 = 7.4686$ ,  $\lambda = 0.0063$ ,  $a = 0.6806$ , and  $N = 0.7381$  were obtained by fitting the measured data with sonication for 400 s in the range of  $\dot{\gamma} > 10$ . The viscosity curve was fitted using the same data (with sonication for 400 s in the range of  $\dot{\gamma} > 10$ ), where the power-law exponent  $n = 0.8951$ . The shear-thinning effect was considered in the viscosity to obtain the stress components in addition to the velocity profile (Eq. (7)). Here,  $\mu = \eta_{CY}$  was used for the stress tensor (Eq. (9)) because the Carreau–Yasuda model (red solid red line in Fig. 2) is better for fitting experimental data than a power-law model (blue dotted line in Fig. 2).

### 3.1.2 Photoelastic measurement of radial Hele-Shaw flow

The experimental setup for the photoelastic measurements of radial Hele-Shaw flow is shown in Fig. 3. The radial Hele-Shaw cell consists of two soda-lime glass plates (140 mm  $\times$  140 mm, Furukawa Science and Engineering). The upper glass plate has a small hole (4 mm diameter) in its center for liquid injection. These two glasses are separated by four triangular metal plates (40 mm  $\times$  40 mm) placed at the four corners. The thickness of the metal spacers, as measured by a micrometer (Mitutoyo, Digimatic micrometer, MPC-25MX) was  $0.283 \pm 0.012$  mm. These measurements were taken at three different locations for each spacer. The glass plates and spacers of the Hele-Shaw cell were fixed with a flange. The CNC suspension was injected from the upper side of the Hele-Shaw cell using a syringe pump (YSP-301(450258), YMC) with a constant flow rate  $Q$ , where  $Q$  was varied from 25–50 ml/min at intervals of 5 ml/min. This condition was adopted as the condition under which the interface spreads while maintaining a relatively circular shape. Three measurements were conducted for each condition to ensure reliability and reproducibility. Circularly polarized light from a light source with wavelength  $\lambda = 543$  nm (SOLIS-565C, Thorlabs) passed through the linear polarizer and a quarter-wave plate was emitted through the flow field. Elliptically polarized light with retardation and azimuth was then captured by a polarization camera

(CRYSTA PI-5WP, Photron) placed under the Hele-Shaw cell at a frame rate of 250 fps and spatial resolution of 226  $\mu\text{m}/\text{pixel}$ . The photoelastic measurements were performed at room temperature of 22°C. The phase retardation was calculated from the intensity using Eq. (4) in the CRYSTA Stress Viewer software (Photron).

To validate the photoelastic measurements, the phase retardation of a polarizer with known retardation of 50.8 nm and 126.2 nm was measured. An 11 mm  $\times$  11 mm area of the polarizer was selected and 10 line profiles were acquired in the  $x$ -direction at equal intervals. The mean and standard deviation of the phase retardation are shown in Fig. 3(b). From these results, the measurement error was  $-4.96\%$  ( $-2.52$  nm) in the case of 50.8 nm retardation and  $1.27\%$  (1.61 nm) in the case of 126.2 nm retardation. An example of a raw image of the Hele-Shaw flow is shown in Fig. 3(c). The interface shape and interface velocity were evaluated from such raw images. The image analysis process is described in Appendix A.

## 3.2 Preliminary experiments

### 3.2.1 Rheo-optical measurements

To evaluate the stress-optic coefficient  $C_2$ , photoelastic measurements were obtained using a rheometer. The experimental setup is shown in Fig. 4. A parallel-plate type rheometer (MCR302, Anton Paar) with a transparent plate (PP43/GL-HT, Anton Paar) and a stage (PTD200/GL, Anton Paar) was used, with the gap  $d$  set to 0.3 mm. A ring-shaped light source with wavelength  $\lambda = 543$  nm (LDR70SE2, CCS) was mounted on the rheometer. The light passed through the linear polarizer and a quarter-wave plate was emitted through the flow field. The phase retardation was measured by a polarization camera (CRYSTA PI-5WP, Photron) placed under the rheometer at a frame rate of 250 fps in the steady state. The measured data from 100 frames were averaged in time. The spatial resolution was 40  $\mu\text{m}/\text{pixel}$ . Photoelastic measurements were performed at 20°C, as controlled by a temperature system on the rheometer. The calculations based on Eq. (4) using the CRYSTA Stress Viewer software (Photron) were analyzed using ImageJ and MATLAB (R2023b).

The stress-optic coefficient  $C_2$  can be obtained by considering the second-order SOL in rheo-optical measurements under Couette flow in a rheometer. The stress tensor in a rheometer  $\mathbf{T}_{\text{rheo}}$  is as follows:

$$\mathbf{T}_{\text{rheo}} = \begin{pmatrix} -p & 0 & -Ay \\ 0 & -p & Ax \\ -Ay & Ax & -p \end{pmatrix}, \quad (12)$$

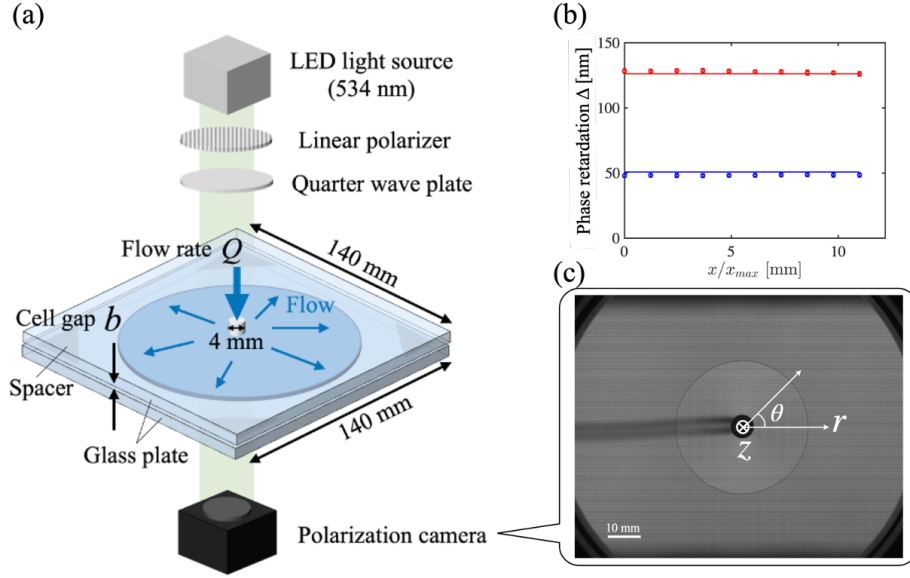


Fig. 3: (a) Experimental setup using Hele-Shaw cell. (b) Measured phase retardation of retarder with  $\Delta = 50.8$  and 126.2 nm. (c) Example of raw image

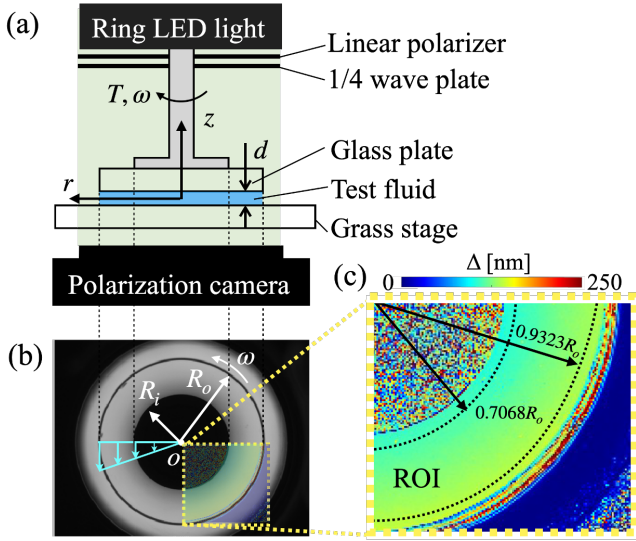


Fig. 4: (a) Experimental setup for rheo-optical measurements, consisting of high-speed polarization camera and a rheometer with a glass parallel plate and stage.  $T$  is torque,  $\omega$  is angular velocity. Plate diameter is  $2R_o = 43.016$  mm. (b) Example of raw image and (c) diagram of a quarter area of phase retardation distribution for  $\dot{\gamma} = 1000$  s $^{-1}$ . Region of interest (ROI) is shown. The phase retardation in the ROI was used to calculate  $C_2$  (Eq. (13))

where  $A = -2T/\pi R_o^4$ ,  $T$  is the torque measured by the rheometer, and  $R_o$  is the plate radius (see Appendix B). These stress components are substituted into Eqs. (2) and (3), from which we obtain the following rela-

tionship:

$$C_2 = \frac{\Delta}{d} \cdot \frac{\pi^2 R_o^6}{4T^2} \cdot \left( \frac{\dot{\gamma}_{\max}}{\dot{\gamma}(r)} \right)^2. \quad (13)$$

where  $\dot{\gamma}$  is the shear rate and  $\dot{\gamma}_{\max} = \dot{\gamma}(R_o)$  is the maximal shear rate at  $r = R_o$ .

The measured flow birefringence for various shear rates is shown in Fig. 5(a) and plotted in Fig. 5(b) as a function of shear rate. As the shear rate changes in the radial direction because of the parallel plates, the phase retardation for a certain range of shear rates can be obtained from a single measurement. The different colors in Fig. 5(b) indicate results with different shear rate settings.

According to Worby et al. (2024), the coefficient of the second term of the SOL ( $C_2$ ) is a function of the second invariant of the deformation tensor. To consider the contribution of three-dimensional effects of the stress field, where the stress components act in the direction of light propagation,  $C_2$  should be expressed as a function of the shear rate. Fitting of the measured data gives the following relationship:

$$C_2 = \alpha |\dot{\gamma}|^\beta, \quad (14)$$

where  $\alpha = 0.0061$ ,  $\beta = -0.7862$ . Worby et al. (2024) reported that the fitting parameters were  $\alpha = 4.4 \times 10^{-6}$  and  $\beta = -0.7862$ , and stated that  $\alpha$  is a function of the concentration of rod particles, indicating a birefringent material. The difference between the values of  $\alpha$  and  $\beta$  obtained in the present study and those reported by Worby et al. (2024) is likely to be caused by differences

in particle alignment due to the different sizes of rod particles, especially length.

Based on these results, the coefficient  $C_2$  used in the theoretical calculation of the photoelastic retardation (Eqs. (1)–(3)) was given by Eq. (14) so that  $C_2$  was a function of the shear rate.

From Fig. 5, the phase retardation increases with increasing shear rate. This is because the CNC particles align with the flow direction. As the alignment of the CNC particles reaches the flow direction, the phase retardation asymptotically approaches a constant value. In contrast, the stress-optic coefficient  $C_2$  decreases with increasing shear rate. Although both trends appear to follow a power-law relationship, they do not perfectly conform to a power-law. According to previous studies (Lane et al., 2022; Calabrese et al., 2022; Worby et al., 2024), there is a power-law relation between the phase retardation and the shear rate. However, the measured data do not perfectly follow a power-law relationship. One possible reason for this deviation from the power-law relationship is the particle interactions that occur because of the relatively high concentration compared with previous studies.

### 3.2.2 Time evolution of phase retardation in Hele-Shaw cell

To evaluate the steady state, the time evolution of the retardation field was investigated. Figure 6 shows the time history of phase retardation measured at three fixed positions ( $r = 1.5$  cm, 2.5 cm, and 3.5 cm in the direction of  $\theta = 180^\circ$ ) and the radius of the interface from the center of the inlet. From Fig. 6, phase retardation of approximately 5 nm occurs even in the absence of fluid before the interface passes through the fixed measurement points. This can be interpreted as an optical measurement error. After the interface passes through the fixed measurement points, the phase retardation increases sharply, and then oscillates around a constant value of 5 nm. Similar oscillation amplitudes occur under other conditions. These oscillations are caused by optical measurement error and machinery error associated with the syringe pump. Thus, the phase retardation was time averaged over a 0.5-s period starting 0.5 s after the averaged interface radius reached 35 mm (highlighted in red in Fig. 6).

### 3.2.3 Actual gap evaluation

The interfacial velocity was evaluated, allowing the actual gap at the moment of fluid flow to be estimated (Chen, 1989).

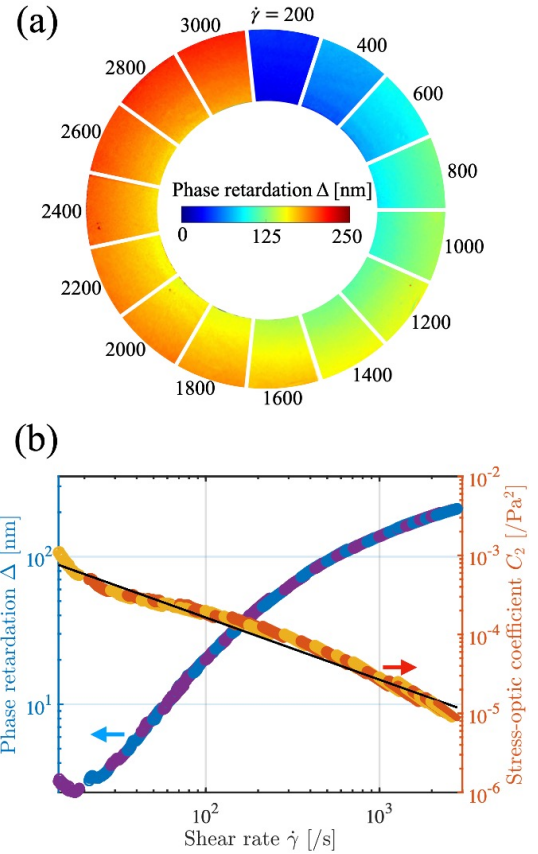


Fig. 5: (a) Phase retardation measured using rheo-optical setup (Fig. 4) for various shear rates. (b) Phase retardation  $\Delta$  and  $C_2$  as a function of shear rate  $\dot{\gamma}$ . Blue and purple plots are measured  $\Delta$  and yellow and red plots are  $C_2$  calculated using Eq. (13). Different plot colors indicate results with different shear rate settings in the rheometer. Black solid line is the fitting curve given by Eq. (14)

First, the bottom-view interface shape was evaluated. The time evolution of the interface for various flow rates is shown in Fig. 7. In the initial phase with a small radius and high interfacial velocity, the test fluid spreads out in concentric rings, regardless of flow rate. As the radius increases and the interface velocity decreases, the interface deviates from the circle, and the deviation becomes more significant for lower flow rates.

To evaluate the interface shape quantitatively, the circularity was evaluated using the distance from the center of the inlet to the interface over  $360^\circ$ . The circularity is defined as

$$c = \frac{r_{\max} - r_{\min}}{2}, \quad (15)$$

where 0.5 denotes perfect circularity and values greater than 0.5 indicate deviation from a circle. The relationship between the interface radius and circularity is shown

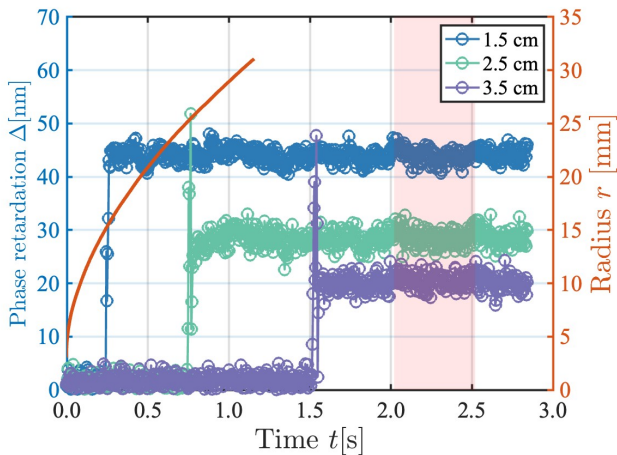


Fig. 6: Time history of phase retardation measured at fixed positions located 1.5 cm, 2.5 cm, and 3.5 cm in the direction of  $\theta = 180^\circ$  from the center of the inlet (in blue, green, purple; left  $y$ -axis) and radius of the flow field (in red; right  $y$ -axis) for  $Q = 50$  ml/min. Region highlighted in red corresponds to the section for which time averaging was applied

in Fig. 8(a). The interface shape deviates from a circle with increasing radius, regardless of flow rate. In addition, the interface shape for low flow rates deviates from a perfect circle, and becomes close to a circle with increasing flow rate. When the pressure gradient decreases with a large radius or low flow rate, the relative magnitude between the pressure gradient and surface tension changes locally. The pressure then increases due to local interface deformation, resulting in deviation from a circular shape. Although the experimental system is different, a similar observation was reported by Suzuki et al. (2019), where they state that the interface becomes stable at high flow rates when the pressure gradient exceeds the thermodynamic body force.

Next, the interface velocity was evaluated. The experimental results are compared with the theoretical solution with  $b = 0.3$  mm in Fig. 8(b). The theoretical solution is given by

$$u_r = \frac{Q}{2\pi r b}. \quad (16)$$

The experimental results are in good agreement with the curve of the radial velocity change in the theoretical solution. However, the value of the measured interface velocity is lower than the theoretical value, regardless of flow rate.

There are two possible reasons why the measured interface velocity is less than the theoretical value: the actual flow rate is lower than the set flow rate and/or the actual gap is larger. For the former, the actual flow

rate was checked and the error was found to be  $-2.0\%$ .

The latter possibility is now discussed. Although the theoretical results were obtained by assuming  $b = 0.3$  mm, which is larger than the measured thickness of the spacer, it is conceivable that the interface velocity was underestimated due to the actual gap being larger. One possible factor in the gap being larger than the measured thickness of the spacer is deformation of the glass caused by the high pressure of injection.

The actual gap was then estimated to minimize the error, and was found to be 0.32 mm. To estimate the actual gap of the flow, the error in the measured velocity was evaluated as follows: The interfacial velocity corresponding to points in the range  $r = 0-35$  mm (at 1.5 mm intervals) were calculated by spline interpolation of the experimental data. The results from three measurements under each condition at the same  $r$  point were averaged, and the difference between the interpolated velocity and the theoretical value was obtained. Finally, all errors in the range  $15 \text{ mm} < r < 35 \text{ mm}$  for all flow conditions were averaged, and the result was defined as  $e$ . The averaged error  $e$  for all flow rates is shown in Fig. 8(c). The linear approximation is represented as  $e = 310.89b - 100$ . The actual gap can be estimated as  $b$ , where the difference between the measured interface velocity and that of the theoretical solution has been minimized. Consequently, the actual gap corresponds to the intersection of the fitted line with  $e = 0$ , which was determined to be 0.32.

## 4 Results and Discussion

### 4.1 Results

Figure 9 depicts snapshots of the phase retardation distribution in the radial Hele-Shaw cell for various flow rates at the end of the averaging period. The phase retardation decreases in the radial direction for all cases and increases with increasing flow rate. When the interface shape deviates from a perfect circle, the local phase retardation is affected.

Based on the results presented so far, the spatiotemporally averaged phase retardation is compared with the theoretical results. Figure 10(a) compares the experimental data (plots) with the theoretical solution assuming a non-Newtonian fluid with  $b = 0.3$  mm (solid and dotted lines). The dotted line indicates the theoretical solution under the assumption of  $C_2 = 0$ , which corresponds to the solution with the conventional SOL. The theoretical results with  $C_2 = 0$  are of  $O(10^{-6})$ . In Hele-Shaw flow, the stress components  $\sigma_{xz}$  are much larger than  $\sigma_{xx}$  and  $\sigma_{yy}$ ; therefore, the effects of  $C_2$

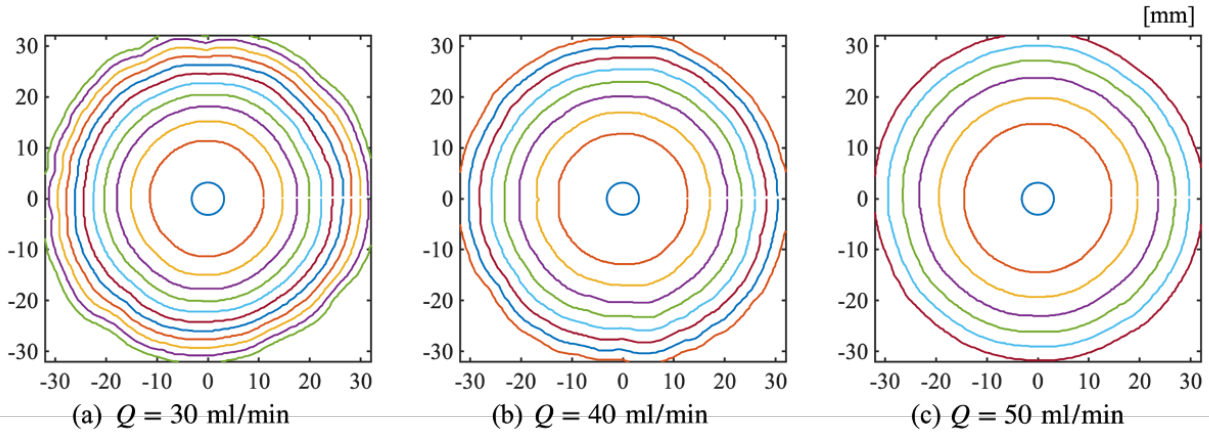


Fig. 7: Time evolutions of interface for various flow rates. The different colors correspond to a time interval of 0.2 s. (a)  $Q = 30$  ml/min, (b)  $Q = 40$  ml/min, (c)  $Q = 50$  ml/min

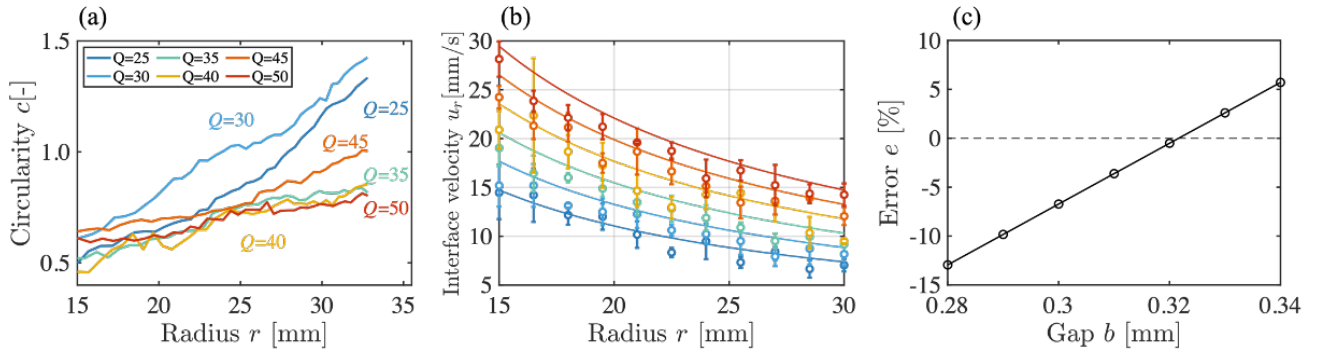


Fig. 8: (a) Circularity of interface shape for various flow rates. (b) Interface velocity for various flow rates. Solid lines are the theoretical solution (Eq. (16)) with  $b=0.3$  mm and plots are experimental results. Error bar indicates  $\pm 1\text{SD}$ . (c) Averaged error  $e$  for various gaps  $b$ . The best fit is  $e = 310.89b - 100$ . The intersection with  $e = 0$  occurs at  $b = 0.322$

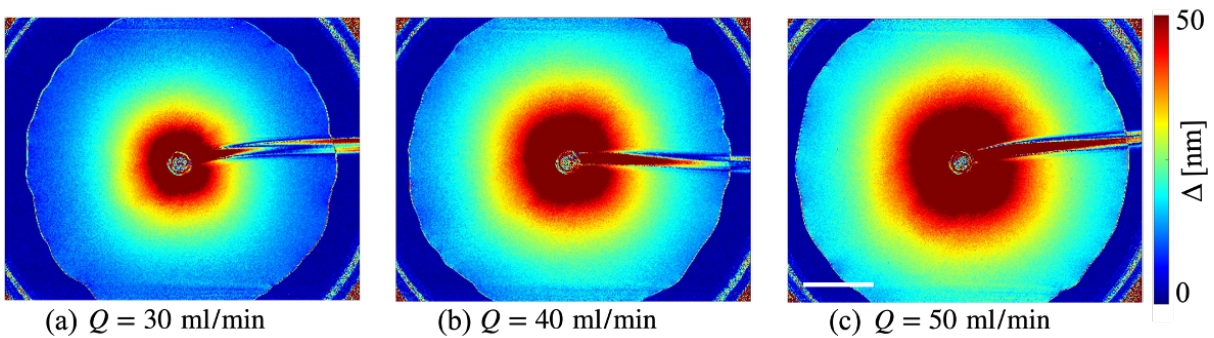


Fig. 9: Examples of measured phase retardation distribution in Hele-Shaw cell for various flow rates at the end of the temporal averaging period (highlighted in Fig. 6). White bar indicates scale for 20 mm. (a)  $Q = 30$  ml/min,  $t = 3.64$  s, (b)  $Q = 40$  ml/min,  $t = 2.85$  s, (c)  $Q = 50$  ml/min,  $t = 2.52$  s

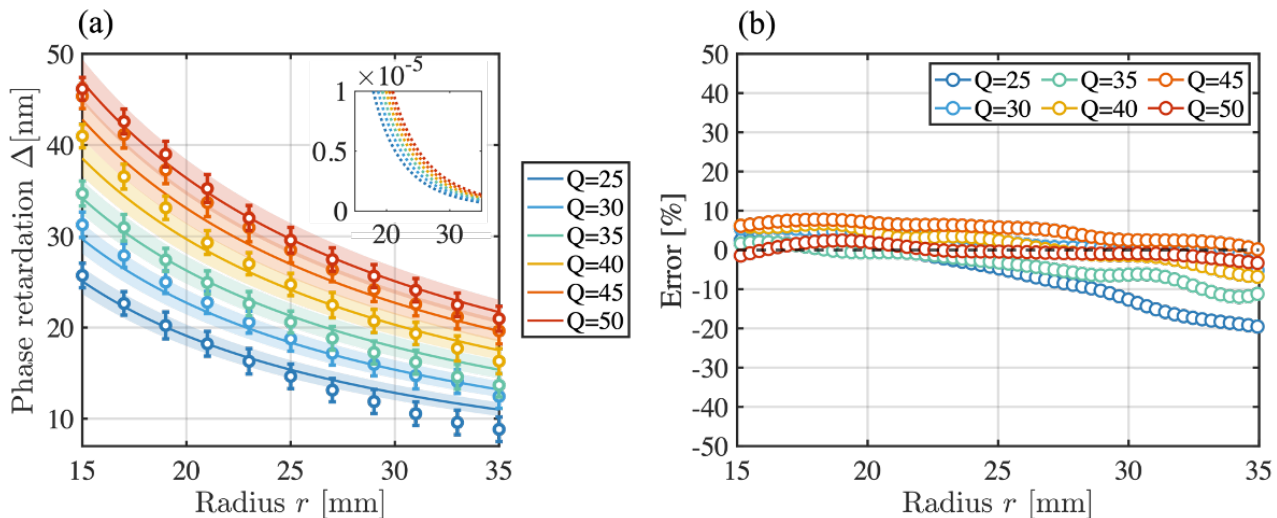


Fig. 10: (a) Phase retardation in radial direction with theoretical results considering shear-thinning effects for  $b = 0.3$  (solid line) and experimental results (plots) for various flow rates  $Q = 25\text{--}50$  ml/min at intervals of 5 ml/min. Solid lines are theoretical solutions with fitted  $C_2$  and dotted lines are those with  $C_2 = 0$  (inset). Shaded area represents the range  $b = 0.28\text{--}0.32$  mm. (b) Error between experimental and theoretical results in radial direction assuming shear-thinning fluid

are dominant over those of  $C_1$ . This suggests that the conventional SOL cannot capture the phase retardation in Hele-Shaw flow. The solid line indicates the theoretical solution with  $C_2$  as a function of shear rate, as estimated from the rheo-optical measurements (§3.2.1). The experimental results are in good quantitative agreement with the theoretical results.

To compare the experimental and theoretical results more quantitatively, Fig. 10(b) illustrates the error between them under the assumption of a non-Newtonian fluid using the second-order SOL.

In the case of a lower shear rate (lower flow rate case and region with larger  $r$ ), the theoretical solution gives an overestimate. One possible reason is that the viscosity is overestimated for the lower shear rate. The phase retardation becomes small farther from the center, and then the optical errors become relatively large. In addition, as the radius increases, the deviation from the perfect circle increases (Fig. 8), and the error grows due to the interface deviating from a circle.

In summary, the experimental phase retardation of shear-thinning fluid in a radial Hele-Shaw cell has been quantitatively explained using the theoretical solution based on the second-order SOL. This incorporates the modeling of non-Newtonian properties and considers  $C_2$  as a function of shear rate based on rheo-optical measurements. To the best of our knowledge, these results are the first quantitative experimental measurements of flow birefringence in Hele-Shaw flow for shear-thinning

fluids. In the following, we discuss the shear-thinning effect in detail.

## 4.2 Discussion

Here, we discuss the dominant influences introduced by shear-thinning. In shear-thinning fluids, unlike Newtonian fluids, the viscous stress or  $C_2$  decreases as the shear rate increases, as shown in Figs. 2 and 5. Consequently,  $V_1$  in Eq. (2) decreases with increasing shear rate. We may then expect the slope of the  $\Delta$ - $r$  curve to decrease when shear-thinning effects are taken into account. In the following, we discuss which aspect of shear-thinning has a dominant effect on phase retardation: (i) the change in stresses or (ii) the variation in the coefficient  $C_2$ .

First, to examine the effects of changes in the viscous stresses, we assume that the only viscosity is a function of the shear rate (Eq. (10)) while maintaining a constant value of  $C_2$ . By evaluating this condition, we can assess the effect of stress variations induced by shear-thinning. The results of this analysis are shown in Fig. 11 (dashed-dotted line). In this case, the representative value of  $C_2$  was obtained by averaging its values over the  $rz$ -cross-section when considered as a function of the shear rate, and using half of this average as the characteristic value to facilitate a comparison of the slope.

Second, to examine the effects of changes in the coefficient  $C_2$ , we assume that only  $C_2$  is a function of the shear rate (Eq. (14)) while keeping the viscosity constant. This approach allows us to assess the impact of variations in  $C_2$ . The results of this evaluation are shown in Fig. 11 (dotted line). Here, the viscosity was assigned the averaged value obtained from the  $r$ - $z$ -cross-section when considered as a function of the shear rate.

In Fig. 11, the solid line represents the case in which both the viscosity and  $C_2$  are functions of the shear rate (Eqs. (10) and (14)), which is same as the solid lines in Fig. 10(a). Comparing this with the cases where viscosity is function of shear rate (dashed-dotted line) and where the  $C_2$  is a function of shear rate (dotted line), we observe that the slope approaches that of the solid line in the latter case. This result suggests that  $C_2$  is the dominant factor in determining the effect of shear-thinning.

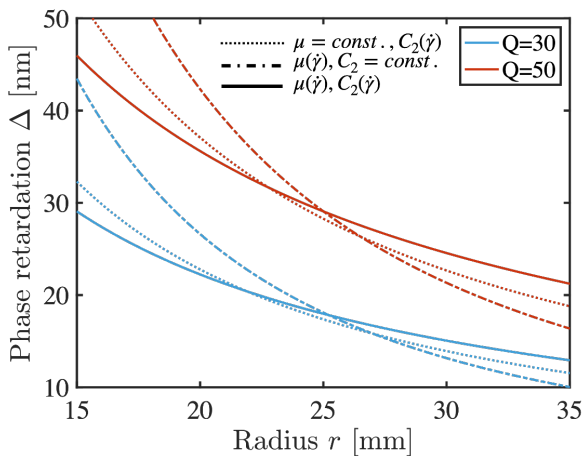


Fig. 11: Theoretical result of phase retardation distribution in radial direction for  $b = 0.3$  mm for flow rates  $Q = 30$  and  $50$  ml/min. The dotted line assumes  $\mu$  is constant and  $C_2$  is a function of shear rate (Eq. (14)). The dashed-dotted line assumes shear-thinning viscosity is a function of shear rate fitted by the Carreau–Yasuda model (Eq. (10)) and  $C_2$  is constant

## 5 Conclusion

We have measured the flow birefringence at various flow rates with CNC suspensions in a steady radial Hele-Shaw flow. The flow birefringence has been investigated, focusing on the effects of stress along the optical direction and the shear-thinning property of the fluid. The measured phase retardation was compared with

the theoretical solution based on the SOL. We found that the conventional SOL does not correctly predict the experimental phase retardation in Hele-Shaw flow, as it neglects the stress along the optical axis. Phase retardation in Hele-Shaw flow, which cannot be described by the conventional SOL, was quantitatively described using the second-order SOL based on rheo-optical measurements. The shear-thinning effect on phase retardation was also discussed. The shear-thinning behavior decreases the spatial gradient of phase retardation in the radial direction. To understand the shear-thinning effect on phase retardation, we considered two aspects: one is change in stress due to a change in the viscosity, and the other one is change in  $C_2$  as a function of shear rate. As a result, the  $C_2$  effect is more significant in terms of the phase retardation distribution in the radial direction. The results of our study will enable a quantitative interpretation of the measured flow birefringence in Hele-Shaw flow.

**Acknowledgements** R. X. S. and Y.T. thank the JST PRESTO (Grant No. JPMJPR22O5), and M.K., R. X. S., Y.N. and Y.T. thank the Sumitomo Foundation (Grant No. 2401115) for financial support; M.K. acknowledges financial support from JSPS KAKENHI (Grant No. JP23K13252), and Y.T. acknowledges financial support from JSPS KAKENHI (Grant No. JP20H00223) and JST PRESTO (Grant No. JPMJPR21O5).

## A Image analysis

To measure the interface shape and velocity, recorded images were processed using MATLAB (R2023b). The key images are illustrated in Fig. A.1. The image processing steps are as follows:

1. Background subtraction: The background of the raw image (Fig. A.1(a)) was subtracted using a reference image before injection without an interface.
2. Gaussian filtering: A Gaussian filter was applied to smooth the image, with the standard deviation set to 0.5.
3. Contrast adjustment: The contrast of the filtered image was adjusted to enhance the visibility of the features.
4. Removing small objects: Objects smaller than a threshold of 1,000 pixels were removed using `bwareaopen` operation (Fig. A.1(b)).
5. Erosion (shrinking objects): Morphological erosion was applied to shrink objects in the image using a disk-shaped structuring element of radius 5 (Fig. A.1(c)).
6. Removing small objects again: Objects smaller than a threshold (based on the size of the circular region from the previous time step) were removed.
7. Dilation (expanding objects): Morphological dilation was applied to expand the remaining objects in the image, restoring them after the erosion step. The holes inside objects were filled using an `imfill` operation.
8. Second erosion step: A second round of morphological erosion was performed with a larger structuring element (disk of radius 30).
9. Filtering regions based on distance from center: Connected components in the image were labeled, and the centroid of

the labeled regions was extracted. The regions were then filtered based on their distance from the center of the inlet. If a region's centroid was within a defined distance threshold (150 pixels), it was retained; otherwise, it was discarded (Fig. A.1(d)).

10. Final dilation and filling: Morphological dilation was applied again to the filtered regions, and the holes in the final image were filled.

Circle detection was applied to the reference image to obtain the center and radius of the inlet. Using the image obtained by image analysis, the distance from the inlet center to the interface was calculated. The radius was averaged over  $360^\circ$ , and the interfacial velocity was calculated from the averaged radius.

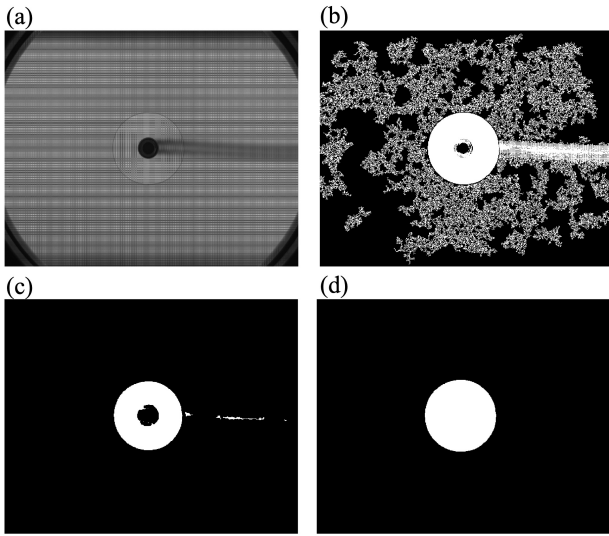


Fig. A.1: Key stages of image analysis: (a) Raw image, (b) background subtraction, Gaussian filtering, contrast enhancement, and small object removal, (c) edge detection, (d) dilation

## B Determination of $C_2$ from rheo-optical measurements

The stress tensor of an incompressible fluid in cylindrical coordinates is (Bird et al., 2002)

$$\mathbf{T}_{r\theta z} = \begin{pmatrix} -p + 2\mu \frac{\partial u_r}{\partial r} & \mu \left( r \frac{\partial}{\partial r} \left( \frac{u_r}{r} \right) + \frac{1}{r} \frac{\partial u_r}{\partial \theta} \right) & \mu \left( \frac{\partial u_r}{\partial z} + \frac{\partial u_z}{\partial r} \right) \\ \mu \left( r \frac{\partial}{\partial r} \left( \frac{u_r}{r} \right) + \frac{1}{r} \frac{\partial u_r}{\partial \theta} \right) & -p + 2\mu \left( \frac{1}{r} \frac{\partial u_\theta}{\partial \theta} + \frac{u_r}{r} \right) & \mu \left( \frac{1}{r} \frac{\partial u_z}{\partial \theta} + \frac{\partial u_\theta}{\partial z} \right) \\ \mu \left( \frac{\partial u_r}{\partial z} + \frac{\partial u_z}{\partial r} \right) & \mu \left( \frac{1}{r} \frac{\partial u_z}{\partial \theta} + \frac{\partial u_\theta}{\partial z} \right) & -p + 2\mu \frac{\partial u_z}{\partial z} \end{pmatrix} \quad (17)$$

In the flow within a rheometer using a parallel plate,  $\frac{\partial}{\partial \theta}$  is zero under the assumption of axial symmetry with respect to the  $z$ -axis. In addition, the velocities  $u_\theta$  and  $u_z$  are assumed to be zero. Then,

$$\mathbf{T}_{r\theta z} = \begin{pmatrix} -p & 0 & 0 \\ 0 & -p & \mu \frac{\partial u_\theta}{\partial z} \\ 0 & \mu \frac{\partial u_\theta}{\partial z} & -p \end{pmatrix} = \begin{pmatrix} -p & 0 & 0 \\ 0 & -p & \frac{2rT}{\pi\mu R_o^4} \\ 0 & \frac{2rT}{\pi\mu R_o^4} & -p \end{pmatrix}, \quad (18)$$

where the velocity  $u_\theta$  in a viscometer with a parallel plate (Bird et al., 1987, pp.37-38) is

$$u_\theta = \frac{r\omega}{d} z = \frac{2rT}{\pi\mu R_o^4} z. \quad (19)$$

Transforming from cylindrical coordinates to Cartesian coordinates, the stress tensor is expressed as

$$\mathbf{T}_{xyz} = \begin{pmatrix} -p & 0 & \frac{2T}{\pi\mu R_o^4} y \\ 0 & -p & -\frac{2T}{\pi\mu R_o^4} x \\ \frac{2T}{\pi\mu R_o^4} y & -\frac{2T}{\pi\mu R_o^4} x & -p \end{pmatrix}. \quad (20)$$

Finally, we define  $\mathbf{T}_{xyz} = \mathbf{T}_{\text{rheo}}$ .

## References

- Aben H, Guillet C (1993) Photoelasticity of glass. Springer Science & Business Media
- Aben H, Puro A (1997) Photoelastic tomography for three-dimensional flow birefringence studies. *Inv Probl* 13(2):215
- Batchelor GK (2000) An introduction to fluid dynamics. Cambridge University Press
- Bird R, Stewart W, Lightfoot E (2002) Transport Phenomena, 2nd ed. Wiley Text Books, New York, NY, USA
- Bird RB, Armstrong RC, Hassager O (1987) Dynamics of polymeric liquids. Vol. 1: Fluid mechanics. John Wiley and Sons Inc., New York, NY
- Bischofberger I, Ramachandran R, Nagel SR (2014) Fingering versus stability in the limit of zero interfacial tension. *Nat Commun* 5(1):5265
- Calabrese V, Varchanis S, Haward SJ, Shen AQ (2022) Alignment of colloidal rods in crowded environments. *Macromolecules* 55(13):5610–5620
- Cerf R, Scheraga HA (1952) Flow birefringence in solutions of macromolecules. *Chem Rev* 51(2):185–261
- Chen JD (1989) Growth of radial viscous fingers in a hele-shaw cell. *J Fluid Mech* 201:223–242
- Decruppe J, Ponton A (2003) Flow birefringence, stress optical rule and rheology of four micellar solutions with the same low shear viscosity. *Eur Phys J E* 10:201–207
- Delon LC, Guo Z, Kashani MN, Yang CT, Prestidge C, Thierry B (2020) Hele-Shaw microfluidic device: A new tool for systematic investigation into the effect of the fluid shear stress for organs-on-chips. *MethodsX* 7:100980
- Deshmukh K, Arlov D, Cant R, Göransson A, Innings F, Wilson DJ (2022) Cleaning of simple cohesive soil layers in a radial flow cell. *Food Bioprod Process* 136:84–96
- Doyle JF (1982) On a nonlinearity in flow birefringence. *Exp Mech* 22:37–38
- Ehyaedi D, Kiger KT (2014) Quantitative velocity measurement in thin-gap Poiseuille flows. *Exp Fluids* 55:1–12
- Goldstein AS, DiMilla PA (1998) Comparison of converging and diverging radial flow for measuring cell adhesion. *AICHE J* 44(2):465–473

- Hele-Shaw HS (1898) Flow of water. *Nature* 58(1509):520–520
- Homsy GM (1987) Viscous fingering in porous media. *Annu Rev Fluid Mech* 19(1):271–311
- Hu DL, Goreau TJ, Bush JW (2009) Flow visualization using tobacco mosaic virus. *Exp Fluids* 46:477–484
- Kloosterman A, Poelma C, Westerweel J (2011) Flow rate estimation in large depth-of-field micro-PIV. *Exp Fluids* 50:1587–1599
- Lajeunesse E, Martin J, Rakotomalala N, Salin D (1997) 3D instability of miscible displacements in a Hele-Shaw cell. *Phys Rev Lett* 79(26):5254
- Lajeunesse E, Martin J, Rakotomalala N, Salin D, Yortsos Y (1999) Miscible displacement in a hele-shaw cell at high rates. *Journal of Fluid Mechanics* 398:299–319
- Lane C, Rode D, Rösgen T (2022) Birefringent properties of aqueous cellulose nanocrystal suspensions. *Cellulose* 29(11):6093–6107
- Lane C, Baumann F, Rode D, Rösgen T (2024) Two-dimensional strain rate imaging study using a polarization camera and birefringent aqueous cellulose nanocrystal suspensions. *Exp Fluids* 65(1):8
- Macosko CW (1994) *Rheology principles*. VCH Publishers
- Marin A, Rossi M, Rallabandi B, Wang C, Hilgenfeldt S, Kähler CJ (2015) Three-dimensional phenomena in microbubble acoustic streaming. *Phys Rev Appl* 3(4):041001
- Maxwell JC (1874) On double refraction in a viscous fluid in motion. *Proc R Soc Lond* 22:46–47
- Nakamine K, Yokoyama Y, Worby WKA, Muto M, Tagawa Y (2024) Flow birefringence of cellulose nanocrystal suspensions in three-dimensional flow fields: Revisiting the stress-optic law. *Cellulose* 31(12):7405–7420
- Nand S, Sharma V, Das SK, Padhee SS, Mishra M (2022) Effect of Hele-Shaw cell gap on radial viscous fingering. *Sci Rep* 12(1):18967
- Noto D, Tasaka Y, Hitomi J, Murai Y (2020) Applicability evaluation of the stress-optic law in Newtonian fluids toward stress field measurements. *Phys Rev Res* 2(4):043111
- Ober TJ, Soulagés J, McKinley GH (2011) Spatially resolved quantitative rheo-optics of complex fluids in a microfluidic device. *J Rheol* 55(5):1127–1159
- Oliveira RM, Meiburg E (2011) Miscible displacements in Hele-Shaw cells: three-dimensional Navier–Stokes simulations. *J Fluid Mech* 687:431–460
- Onuma T, Otani Y (2014) A development of two-dimensional birefringence distribution measurement system with a sampling rate of 1.3 MHz. *Opt Commun* 315:69–73
- Otani Y, Shimada T, Yoshizawa T, Umeda N (1994) Two-dimensional birefringence measurement using the phase shifting technique. *Opt Eng* 33(5):1604–1609
- Pindera J, Krishnamurthy A (1978) Characteristic relations of flow birefringence: Part 1: Relations in transmitted radiation. *Exp Mech* 18:1–10
- Prabhakaran R (1975) On the stress-optic law for orthotropic-model materials in biaxial-stress fields. *Exp Mech* 15:29–34
- Ramesh K (2021) *Developments in Photoelasticity: A renaissance*. IOP Publishing
- Rankin G, Sabbah H, Stein P (1989) A streaming birefringence study of the flow at the junction of the aorta and the renal arteries. *Exp Fluids* 7(2):73–80
- Rezania A, Thomas CH, Healy KE (1997) A probabilistic approach to measure the strength of bone cell adhesion to chemically modified surfaces. *Ann Biomed Eng* 25:190–203
- Robert L, Vergnes B, Demay Y (2003) Flow birefringence study of the stick–slip instability during extrusion of high-density polyethylenes. *J Non-Newton Fluid Mech* 112(1):27–42
- Saffman PG, Taylor GI (1958) The penetration of a fluid into a porous medium or Hele-Shaw cell containing a more viscous liquid. *Proc R Soc Lond Ser A Math Phys Sci* 245(1242):312–329
- Sato T, Yamagata Y, Sato Y, Onuma T, Miyamoto K, Takahashi T (2024) Two-dimensional rheo-optical measurement system to study dynamics and structure of complex fluids. *Appl Rheol* 34(1):20240006
- Shafiei-Sabet S, Hamad WY, Hatzikiriakos SG (2012) Rheology of nanocrystalline cellulose aqueous suspensions. *Langmuir* 28(49):17124–17133
- Sun CL, Huang HY (2016) Measurements of flow-induced birefringence in microfluidics. *Biomicrofluidics* 10(1):011903
- Sun YD, Sun YF, Sun Y, Xu X, Collins M (1999) Visualisation of dynamic flow birefringence of cardiovascular models. *Opt Laser Technol* 31(1):103–112
- Suzuki RX, Nagatsu Y, Mishra M, Ban T (2019) Fingering pattern induced by spinodal decomposition in hydrodynamically stable displacement in a partially miscible system. *Phys Rev Fluids* 4(10):104005
- Videbæk TE, Nagel SR (2019) Diffusion-driven transition between two regimes of viscous fingering. *Phys Rev Fluids* 4(3):033902
- Winter HH (1975) Approximate calculation and measurement of the pressure distribution in radial flow of molten polymers between parallel discs. *Polym Eng Sci* 15(6):460–469
- Worby WKA, Nakamine K, Yokoyama Y, Muto M, Tagawa Y (2024) Examination of flow birefringence induced by the shear components along the optical axis using a parallel-plate-type rheometer. *Sci Rep* 14(1):21931
- Yang Z, Yortsos YC (1997) Asymptotic solutions of miscible displacements in geometries of large aspect ratio. *Phys Fluids* 9(2):286–298
- Yasuda K, Armstrong R, Cohen R (1981) Shear flow properties of concentrated solutions of linear and star branched polystyrenes. *Rheol Acta* 20(2):163–178
- Zhang X, Rallabandi B (2023) Three-dimensional streaming around an obstacle in a Hele-Shaw cell. *J Fluid Mech* 961:A35
- Zhao Y, Shen AQ, Haward SJ (2016) Flow of wormlike micellar solutions around confined microfluidic cylinders. *Soft Matter* 12(42):8666–8681